

C.G. Pappas, J.W. Fowler, D.A. Bennett, W.B.
Doriese, Y.I. Joe, K.M. Morgan, G.C. O'Neil,
J.N. Ullom, D.S. Swetz

A Highly Linear Calibration Metric for TES X-ray Microcalorimeters

the date of receipt and acceptance should be inserted later

Abstract Transition-edge sensor X-ray microcalorimeters are usually calibrated empirically, as the most widely-used calibration metric, optimal filtered pulse height (OFPH), in general has an unknown dependence on photon energy, E_γ . Because the calibration function can only be measured at specific points where photons of a known energy can be produced, this unknown dependence of OFPH on E_γ leads to calibration errors and the need for time-intensive calibration measurements and analysis. A calibration metric that is nearly linear as a function of E_γ could help alleviate these problems. In this work, we assess the linearity of a physically motivated calibration metric, E_{Joule} . We measure calibration pulses in the range $4.5 \text{ keV} < E_\gamma < 9.6 \text{ keV}$ with detectors optimized for 6 keV photons to compare the linearity properties of E_{Joule} to OFPH. In these test data sets, we find that E_{Joule} fits a linear function an order of magnitude better than OFPH. Furthermore, calibration functions using E_J , an optimized version of E_{Joule} , are linear within the 2-3 eV noise of the data.

Keywords Microcalorimeter, Transition-edge sensor (TES), Detector calibration, X-ray spectroscopy

1 Introduction

The transition-edge sensor (TES) microcalorimeter is capable of detecting single photons with energy resolving powers exceeding 1000. It can be optimized for use in the soft X-ray, hard X-ray, or gamma ray regime¹. TES microcalorimeters have been used for a variety of applications², including particle-induced X-ray emission (PIXE)³, time-resolved chemistry^{4,5}, nuclear forensics⁶, and hadronic atom studies⁷. Other experiments in development include instruments for indirect measurement of the neutrino mass⁸ and orbiting astronomical telescopes^{9,10,11}.

Quantum Sensors Group, NIST Boulder Laboratories, 325 Broadway, MS 687.08, Boulder, Colorado 80305, USA. Tel: +1 303-497-3874.
E-mail: christine.pappas@nist.gov

In all these applications, the TES microcalorimeter requires a calibration procedure to map the directly measured signal, a time record of the pulse in the TES current, into the desired quantity: photon energy (E_γ). Various calibration metrics can be calculated from the TES current pulse as a function of E_γ to generate a calibration function. The most commonly used metric is the optimal filtered pulse height (OFPH), a low-noise estimator of the pulse size^{12 13}.

When pulse signals are very small, the detector properties remain at their quiescent values during the pulse. In this small-signal limit, the pulse shape is constant with a size proportional to E_γ , and the OFPH is proportional to E_γ . However, a TES microcalorimeter can only be designed to remain in the small-signal limit over a large energy range at the sacrifice of energy resolution.

In reality, the OFPH calibration function has a complicated shape that is determined completely empirically. It can only be measured at select points where photons can be generated with known energies. The calibration function must then be interpolated (and extrapolated) smoothly between (and beyond) these measured “anchor points”. Even when there are anchor points close to the unknown energy and careful interpolation procedures are used, calibration done in this way can be the leading source of systematic uncertainty on absolute line energies¹⁴.

A metric with a known dependence on E_γ (up to some fitting parameters) could produce more accurate calibrations, reduce requirements on anchor points, and simplify calibration analysis. This has led to research into calibration metrics that are more linear than OFPH as a function of E_γ ^{15 16 17 18}. In this paper, we discuss a calibration metric, E_{Joule} , that is nearly proportional to E_γ when applied to our hard X-ray detectors under typical operating conditions. We also discuss a slight adjustment to E_{Joule} that produces the more linear E_J metric. We concern ourselves only with the definition and linearity properties of E_{Joule} and E_J . The direct application to individual, noisy pulse records of the formulas here will yield linear, but highly noisy estimations of E_γ . We treat the problem of their statistically optimal estimation in a companion paper in these same proceedings¹⁹.

2 The E_{Joule} Metric

A TES microcalorimeter measures the energy of individual photons. The photon is absorbed by an “island” that is only weakly thermally connected to a silicon substrate held at constant temperature, T_{bath} . The signal resulting from an absorbed photon is a downward pulse in the current through the voltage-biased TES on the island. The shape of this signal depends on the thermal properties of the detector, the electrical properties of the TES bias and readout circuits, and the resistive transition function of the TES with respect to temperature and current, $R(T, I)$. Here, we parameterize the $R(T, I)$ function by the TES normal resistance (R_n), the TES critical temperature (T_c), and the local logarithmic derivatives of $R(T, I)$ with respect to temperature and current: $\alpha(T, I)$ and $\beta(T, I)$.

To define the E_{Joule} metric, which is also referred to as E_{ETF} ^{20 18}, we start with the standard “one-body” thermal model describing this system^{20 21}:

$$P_\gamma = P_{\text{bath}} - P_{\text{Joule}} + C \frac{dT}{dt}, \quad (1)$$

where P_{Joule} is the electrical power generated by the current through the TES, P_γ is the photon power deposited on the TES island, C is the total heat capacity of the TES island, and T is the TES temperature, and P_{bath} is the thermal power flowing from the TES island to the bath. This quantity is usually modeled as a power-law:

$$P_{\text{bath}} = \kappa(T^n - T_{\text{bath}}^n), \quad \frac{dP_{\text{bath}}}{dT} = G(T) = \kappa n T^{n-1}, \quad (2)$$

where κ and n are constants.

Integrating Eq. 1 over the duration of the pulse (from t_0 to t_f) yields an expression for the photon energy:

$$E_\gamma = E_{\text{bath}} + E_{\text{Joule}} = \int_{t_0}^{t_f} (P_{\text{bath}} - P_{\text{Joule}}) dt = \int_{t_0}^{t_f} (\Delta P_{\text{bath}} - \Delta P_{\text{Joule}}) dt. \quad (3)$$

The final term of Eq. 1 integrates to zero because the temperature is the same before and after the pulse. When there are no photons incident on the detector, P_{bath} is equal to P_{Joule} . Therefore, we can also write Eq. 3 as shown on the right, where ΔP_{bath} and ΔP_{Joule} are the deviations of P_{bath} and P_{Joule} from their common quiescent value. We define the two positive quantities, E_{bath} and E_{Joule} , as the integrals of ΔP_{bath} and $-\Delta P_{\text{Joule}}$, respectively, over the course of the pulse.

Our TESs are nearly voltage-biased to provide negative electrothermal feedback by applying a constant bias current, I_{bias} , to the TES in parallel with a relatively small shunt resistor, R_{sh} . The TES current is coupled to a SQUID in a flux-locked loop, then amplified²². We directly measure changes in the feedback current necessary to keep the SQUID on its lockpoint, I_{FB} , which we scale by a proportionality constant, M_r , to yield changes in the TES current, I : $\delta I = M_r \delta I_{FB}$. Inductance is often added in series with the TES to slow the current signal for ease of readout. We refer to the total inductance in the bias circuit as L . For a TES in this bias configuration, ΔP_{Joule} is given by the following expression:

$$\Delta P_{\text{Joule}} = R_{\text{sh}} (\delta I (I_{\text{bias}} - 2I_0) - \delta I^2) - (I_0 + \delta I) \frac{d(\delta I)}{dt} L, \quad (4)$$

where I_0 is the quiescent value of the TES current before the pulse and $\delta I = I - I_0$. Integrating over the course of the pulse gives the following expression for E_{Joule} :

$$E_{\text{Joule}} = -R_{\text{sh}} \left[(I_{\text{bias}} - 2I_0) \int_{t_0}^{t_f} \delta I dt - \int_{t_0}^{t_f} (\delta I)^2 dt \right]. \quad (5)$$

The inductance term in Eq. 4 integrates to zero because the energy stored in the inductor is the same before and after the pulse.

One could in principle determine the energy of a photon absorbed by the detector with no need for a calibration curve by calculating both E_{bath} and E_{Joule} from the pulse signal (Eq. 3). The E_{bath} term may be calculated by measuring the thermal conductivity constants κ and n and calculating the temperature of the TES at every point during the pulse (Eq. 2). Although the detector is not in thermal equilibrium during the pulse, the TES temperature can be determined from its previously measured $R(T, I)$ transition function (assuming the function $T(R, I)$ is single-valued and can be measured over the entire transition region the pulse

will traverse). In practice, we have found that using our standard detector characterization techniques, E_γ can be estimated to about $\pm 5\%$ with this method, while many experiments would require precision on the order of $\pm 0.1\%$. We have not yet explored the fundamental limits of this method’s precision, which may be constrained by how precisely it is possible to measure detector parameters and thermal “two-body” effects arising from the finite thermal conductivity between the TES and absorber²¹.

In contrast, calculation of the E_{Joule} term up to a proportionality constant only requires knowledge of the quantities I_{bias} , I_0 , and M_r , which in principle can all be determined to high precision with simple measurements. Although E_{Joule} only approaches E_γ in the infinite loop gain ($\mathcal{L} = \frac{P_{\text{Joule}}\alpha}{GT}$), small signal limit, we find under many conditions that E_{Joule} is nearly proportional to E_γ . In these cases, E_{Joule} is useful as a highly linear calibration metric.

3 Linearity of the E_{Joule} Metric: Simulations

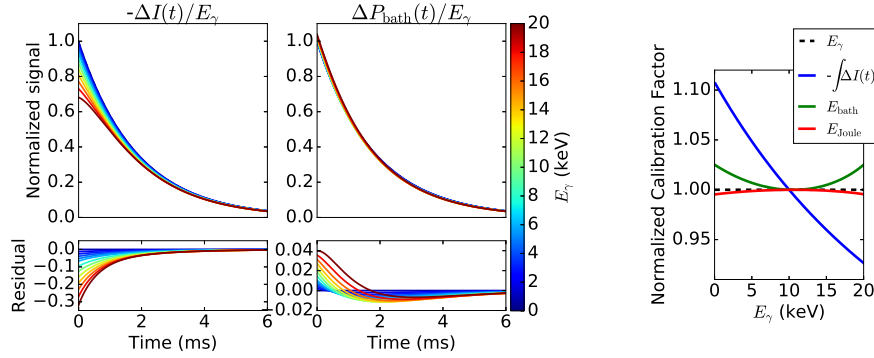


Fig. 1 *Left:* Simulated pulses in $\Delta I/E_\gamma$ and $\Delta P_{\text{bath}}/E_\gamma$ space using the model described in the text. Residuals are taken with respect to the 1 keV photon signal. *Right:* The calibration factor is the metric divided by E_γ , then scaled to equal 1.0 at 10.0 keV. (Color figure online)

When signals are large enough that OFPH is no longer a linear calibration metric, the non-linearized electrical and thermal differential equations describing the detector system must be solved to describe the response of a TES microcalorimeter to an absorbed photon²⁰. Because the solutions are difficult to describe analytically, in this section we explore the linearity of the E_{Joule} metric through simulations of our typical TES hard X-ray microcalorimeters. For intuition-building purposes, we will consider the curvature of $E_{\text{bath}}(E_\gamma)$ instead of $E_{\text{Joule}}(E_\gamma)$. Because we operate under high loop gain conditions, it is almost always true that $E_{\text{bath}} < E_{\text{Joule}}$. When this is the case, by Eq. 3, the curvature of the $E_{\text{Joule}}(E_\gamma)$ calibration curve is less than or equal to the curvature of $E_{\text{bath}}(E_\gamma)$, where we define the curvature of $F(E_\gamma)$ as $\frac{d^2 F}{dE_\gamma^2} \left(\frac{E_\gamma}{F} \right)^2$.

In our simulation, we use detector parameters of the ar13-9b devices² that produced the data in Section 4 of this paper when possible: $\kappa=4000$ pW/Kⁿ, $n=3.3$, $R_{\text{sh}}=360$ $\mu\Omega$, $T_{\text{c}}=109$ mK, $R_{\text{n}}=12$ m Ω , and $T_{\text{bath}}=65$ mK. We describe the TES $R(T, I)$ function using the Two-Fluid model²³, with parameters that do not reproduce the $R(T, I)$ transitions of the ar13-9b TESs exactly, but yield α and β values typical of these devices in the relevant transition area: $c_{\text{I}} * I_{\text{c0}}=5.0$ mA and $c_{\text{R}}=0.5$. Because L does not affect E_{bath} or E_{Joule} by Eq. 3 and Eq. 5, we choose $L = 0$ for convenience. We approximate the TES heat capacity as a constant value of 0.85 pJ/K, independent of temperature. Simulations using more precise measurements of our detectors' $C(T)$ functions may be included in future publications.

In this model, the TES temperature rises instantaneously by an amount E_{γ}/C after a photon is absorbed, then decreases back to the quiescent temperature. Therefore, the height of the TES temperature pulse height is proportional to E_{γ} . The linear approximation of the P_{bath} pulse height is $G\Delta T$, which is also proportional to E_{γ} . The actual P_{bath} pulse height is very close to this linear approximation, such that it is linear with respect to photon energy within a few percent up to 20 keV (Fig. 1). In contrast, the ΔI pulse height differs from a linear relationship with E_{γ} quite strongly. As shown in Fig. 1, this makes the E_{bath} calibration function much closer to linear than that of the pulse average, $\int -\Delta I(t) dt$. The curvature of $E_{\text{Joule}}(E_{\gamma})$ is even smaller than $E_{\text{bath}}(E_{\gamma})$, because E_{Joule} is about five times larger than E_{bath} .

4 Linearity of the E_{Joule} Metric: Experimental Results

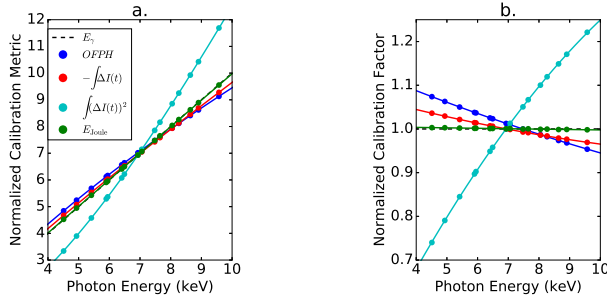


Fig. 2 Example calibration data set from one of the ar13-9b detectors biased at 10% R_{n} with $T_{\text{bath}}=65$ mK. Lines are 3rd order polynomial fits to the data to guide the eye. Fig2a: Various calibration metrics as a function of E_{γ} , normalized as discussed in the text. Fig2b: Data from Fig2a is divided by E_{γ} to yield the Calibration Factor. (Color figure online.)

We have tested the linearity of the E_{Joule} and comparison metrics on calibration data taken with 13 nominally identical ar13-9b X-ray microcalorimeters². These detectors have the same properties used in the simulations above except for the L values, which range from about 90 nH to 500 nH. Calibration data were taken with the detectors operated at a bath temperature of 65 mK at three different bias

points, generating 39 data sets. Each calibration data set consists of averaged pulse signals from photons at the $K\alpha$ and $K\beta$ emission lines of the elements Ti, Cr, Mn, Fe, Co, Ni, Cu, and Zn, which are in the energy range of about 4.5 to 9.6 keV.

A calibration function is produced by applying one of the metrics to a calibration data set. To quantify the linearity of each calibration function in units of eV, we compute a quantity we call linearity- σ as follows. First, we fit the slope of a linear function intersecting the origin to the raw (metric vs. E_γ) calibration function. Then, we divide the metric values by this slope to obtain a normalized calibration function like the one in Fig. 2a. Finally, we compute the root-mean-square deviation of the normalized data set with respect to the $y = x$ line.

As shown in Fig. 3c, the E_{Joule} metric generates calibrations functions with a linearity- σ of 25 eV or less at all bias points tested, an order of magnitude better than OFPH. The E_{Joule} metric is a linear combination of the pulse average and the pulse RMS, $\int (\Delta I)^2 dt$. The pulse average tends to have negative curvature, while the pulse RMS tends to have positive curvature, as shown in Fig. 2. We define the metric E_J as the linear combination of pulse average and pulse RMS that minimizes the linearity- σ of the calibration function: $E_J = A \int -\Delta I dt + B \int \Delta I^2 dt$. The ratio A/B is calculated separately for each detector and bias point. As shown in Fig. 3c, the linearity- σ of the E_J metric is only about 2-3 eV. This is within the noise of this measurement and two orders of magnitude better than that of the OFPH metric.

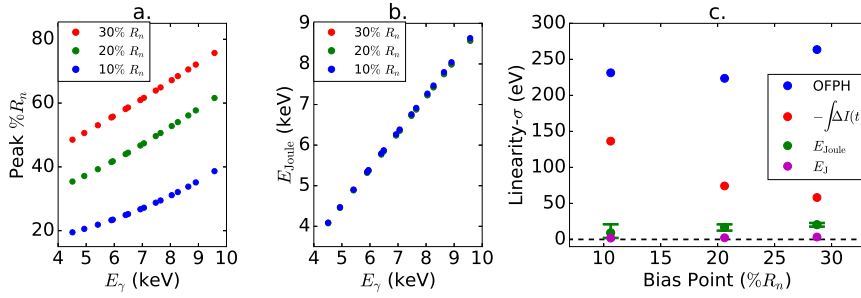


Fig. 3 Calibration data taken with ar13-9b detectors at $T_{\text{bath}}=65$ mK and three different bias points. Fig3a: Data from one of the detectors with L of about 500 nH. For each of the bias points, the TES resistance value at the peak of each pulse is plotted vs. E_γ . Fig3b: Using the same data as in Fig3a, E_{Joule} is calculated and plotted vs. E_γ . Fig3c: For each metric, the linearity- σ , defined in the text, is averaged over the 13 ar13-9b detectors at each bias current, and plotted vs. the average bias $\%R_n$. The systematic error for E_{Joule} is given by the error bars. It is calculated assuming the following measurement errors: $I_{\text{bias}}: \pm 3\%$, $I_0: \pm 5\%$, $M_f: \pm 3\%$. The systematic error in the linearity- σ of the other metrics is zero. The linearity- σ values for the $\int (\Delta I)^2$ metric, not shown, are larger than 1 keV. (Color figure online.)

5 Conclusions and Future Work

We have explored the linearity of two calibration metrics, E_{Joule} and E_J , when applied to hard X-ray TES microcalorimeters under typical operating conditions.

On test data, we have found that the $E_{\text{Joule}}(E_\gamma)$ calibration functions evaluated over 4.5 keV to 9.6 keV fit a linear function an order of magnitude better than OFPH(E_γ). An easy correction to E_{Joule} yields a metric, E_J , that is linear within the 2-3 eV noise of the data.

Because the E_J metric produces nearly linear calibration functions, it may simplify calibration measurements and analysis and produce more accurate results. In a companion paper in this issue, a low-noise estimator of the E_J metric is presented that produces Mn, Co, and Cu $K\alpha$ spectra with energy resolutions comparable to the OFPH results on test data¹⁹. Our next step will be to compare the accuracy and speed of the full calibration procedures using OFPH, the low-noise E_J estimator, and other proposed alternative calibration metrics such as resistance-space^{15 16 17}.

The E_J calibration method could potentially be used for a wide range of TES microcalorimeter applications. As the computational power required for the low-noise E_J estimator is comparable to OFPH, these applications could include X-ray satellite missions. The E_J metric may also be used to develop faster and more robust calibration analysis algorithms. Currently, due to the complexity of the procedure, calibration of data from TES spectrometers is typically performed after the completion of an experiment. The E_J metric could be applied to software in development that will give TES spectrometer users calibrated results in real time to inform their next steps.

Acknowledgements This work was supported by NIST's Innovations in Measurement Science Program and NASA SAT NNG16PT181. C.G.P is supported by the National Research Council Post-Doctoral Fellowship. As this is a contribution of a U.S. Government agency, it is not subject to copyright in the USA.

References

1. J.N. Ullom and D.A. Bennett, *Superconductor Science and Technology* **28**, 084003 (2015).
2. W. B. Doriese, P. Abbamonte, B. K. Alpert, D. A. Bennett, E. V. Denison, Y. Fang, D. A. Fischer, C. P. Fitzgerald, J. W. Fowler, J. D. Gard, J. P. Hays-Wehle, G. C. Hilton, C. Jaye, J. L. Mcchesney, L. Miaja-Avila, K. M. Morgan, Y. I. Joe, G. C. O'Neil, C. D. Reintsema, F. Rodolakis, D. R. Schmidt, H. Tatsuno, J. Uhlig, L. R. Vale, J. N. Ullom, and D. S. Swetz, *Review of Scientific Instruments* **88**, 053108 (2017). doi: 10.1063/1.4983316
3. M. R. J. Palosaari, M. Kyhk, K. M. Kinnunen, M. Laitinen, J. Julin, J. Malm, T. Sajavaara, W. B. Doriese, J. Fowler, C. Reintsema, D. Swetz, D. Schmidt, J. N. Ullom, and I. J. Maasilta, *Phys. Rev. Applied* **6**, 024002 (2016). doi: 10.1103/PhysRevApplied.6.024002
4. L. Miaja-Avila, G. C. O'Neil, Y. I. Joe, B. K. Alpert, N. H. Damrauer, W. B. Doriese, S. M. Fatur, J. W. Fowler, G. C. Hilton, R. Jimenez, C. D. Reintsema, D. R. Schmidt, K. L. Silverman, D. S. Swetz, H. Tatsuno, and J. N. Ullom, *Physical Review X* **6**, 031047 (2016). doi: 10.1103/PhysRevX.6.031047
5. G. C. O'Neil, L. Miaja-Avila, Y. I. Joe, B. K. Alpert, M. Balasubramanian, D. M. Sagar, W. Doriese, J. W. Fowler, W. K. Fullagar, N. Chen, G. C. Hilton, R. Jimenez, B. Ravel, C. D. Reintsema, D. R. Schmidt, K. L. Silverman, D. S.

- Swetz, J. Uhlig, and J. N. Ullom, *The Journal of Physical Chemistry Letters* **8**, 1099 (2017). doi: 10.1021/acs.jpcclett.7b00078
6. M. P. Croce, M. K. Bacrania, E. M. Bond, D. E. Dry, A. L. Klingensmith, W. A. Moody, S. P. Lamont, M. W. Rabin, J. H. Rim, J. A. Beall, D. A. Bennett, V. Kotsubo, R. D. Horansky, G. C. Hilton, D. Schmidt, J. N. Ullom, and R. Cantor, *IEEE Transactions on Applied Superconductivity* **21**, 207 (2011). doi: 10.1109/TASC.2010.2096790
 7. T. Hashimoto, M. Bazzi, D. A. Bennett, C. Berucci, D. Bosnar, C. Curceanu, W. B. Doriese, J. W. Fowler, H. Fujioka, C. Guaraldo, F. P. Gustafsson, R. Hayakawa, R. S. Hayano, J. P. Hays-Wehle, G. C. Hilton, T. Hiraiwa, Y. Ichinohe, M. Iio, M. Iliescu, S. Ishimoto, Y. Ishisaki, K. Itahashi, M. Iwasaki, Y. Ma, H. Noda, H. Noumi, G. C. Oneil, H. Ohnishi, S. Okada, H. Outa, K. Piscicchia, C. D. Reintsema, Y. Sada, F. Sakuma, M. Sato, D. R. Schmidt, A. Scordo, M. Sekimoto, H. Shi, D. Sirghi, F. Sirghi, K. Suzuki, D. S. Swetz, K. Tanida, H. Tatsuno, M. Tokuda, J. Uhlig, J. N. Ullom, S. Yamada, T. Yamazaki, and J. Zmeskal, *IEEE Trans. Appl. Supercond.* **27**, 2100905 (2017). doi: 10.1109/TASC.2016.2646374
 8. A. Giachero, B. Alpert, D. Becker, D. Bennett, M. Biasotti, C. Brofferio, V. Ceriale, G. Ceruti, D. Corsini, P. Day, M. D. Gerone, R. Dressler, M. Faverzani, E. Ferri, J. Fowler, E. Fumagalli, G. Gallucci, J. Gard, F. Gatti, J. Hays-Wehle, S. Heinitz, G. Hilton, U. Kster, M. Lusignoli, J. Mates, S. Nisi, A. Nucciotti, A. Orlando, L. Parodi, G. Pessina, G. Pizzigoni, A. Puiu, S. Ragazzi, C. Reintsema, M. R. Gomes, D. Schmidt, D. Schumann, F. Siccardi, M. Sisti, D. Swetz, F. Terranova, J. Ullom, and L. Vale, *JINST* **12**, C02046 (2017). doi: 10.1088/1748-0221/12/02/C02046
 9. L. Ravera, D. Barret, J. W. D. Herder, L. Piro, R. Cldassou, E. Pointecouteau, P. Peille, F. Pajot, M. Arnaud, C. Pigot, L. Duband, C. Cara, R. H. D. Hartog, L. Gottardi, H. Akamatsu, J. V. D. Kuur, H. J. V. Weers, J. D. Plaa, C. Macculi, S. Lotti, G. Torrioli, F. Gatti, L. Valenziano, M. Barbera, X. Barcons, M. T. Ceballos, L. Fbrega, J. M. Mas-Hesse, M. J. Page, P. R. Guttridge, R. Willingale, S. Paltani, L. Genolet, E. Bozzo, G. Rauw, E. Renotte, J. Wilms, and C. Schmid, *SPIE Astronom. Telescopes + Instr.* **9144**, 91442L (2014). doi: 10.1117/12.2055884
 10. S. J. Smith, J. S. Adams, S. R. Bandler, G. L. Betancourt-Martinez, J. A. Chervenak, M. P. Chiao, M. E. Eckart, F. M. Finkbeiner, R. L. Kelley, C. A. Kilbourne, A. R. Miniussi, F. S. Porter, J. E. Sadleir, K. Sakai, N. A. Wakeham, E. J. Wassell, W. Yoon, D. A. Bennett, W. B. Doriese, J. W. Fowler, G. C. Hilton, K. M. Morgan, C. G. Pappas, C. N. Reintsema, D. S. Swetz, J. N. Ullom, K. D. Irwin, H. Akamatsu, L. Gottardi, R. D. Hartog, B. D. Jackson, J. V. D. Kuur, D. Barret, and P. Peille, *SPIE Astronom. Telescopes + Instr.* **9905**, 99052H (2016). doi: 10.1117/12.2231749
 11. J. A. Gaskin, M. C. Weisskopf, A. Vikhlinin, H. D. Tananbaum, S. R. Bandler, M. W. Bautz, D. N. Burrows, A. D. Falcone, F. A. Harrison, R. K. Heilmann, S. Heinz, R. C. Hopkins, C. A. Kilbourne, C. Kouveliotou, R. P. Kraft, A. V. Kravtsov, R. L. Mcentaffer, P. Natarajan, S. L. O'Dell, R. Petre, Z. R. Prieskorn, A. F. Ptak, B. D. Ramsey, P. B. Reid, A. R. Schnell, D. A. Schwartz, and L. K. Townsley, *UV, X-Ray, and Gamma-Ray Space Instrumentation for Astronomy XIX* **9601**, 96010J (2015). doi: 10.1117/12.2190837

-
12. A.E.Szymkowiak, R.L.Kelley, S.H.Moseley, C.K.Stahle, *J. Low Temp. Phys.* **93**, 281 (1993). doi:10.1007/BF00693433
 13. J. W. Fowler, B. K. Alpert, W. B. Doriese, Y.-I. Joe, G. C. O’Neil, J. N. Ullom, and D. S. Swetz, *J. Low Temp. Phys.* **184**, 374 (2016). doi: 10.1007/s10909-015-1380-0
 14. J. W. Fowler, B. K. Alpert, D. A. Bennett, W. B. Doriese, J. D. Gard, G. C. Hilton, L. T. Hudson, Y.-I. Joe, K. M. Morgan, G. C. O’Neil, C. D. Reintsema, D. R. Schmidt, D. S. Swetz, C. I. Szabo, and J. N. Ullom, *Metrologia* **54**, 494 (2017). doi: 10.1088/1681-7575/aa722f
 15. S. Bandler, E. Figueroa-Feliciano, N. Iyomoto, R. Kelley, C. Kilbourne, K. Murphy, F. Porter, T. Saab, and J. Sadleir, *Nucl. Instr. Meth. Phys. Research A* **559**, 817-819 (2006). doi:10.1016/j.nima.2005.12.149
 16. S. J. Lee, J. S. Adams, S. R. Bandler, J. A. Chervenak, M. E. Eckart, F. M. Finkbeiner, R. L. Kelley, C. A. Kilbourne, F. S. Porter, J. E. Sadleir, S. J. Smith, and E. J. Wassell, *Appl. Phys. Lett.* **107**, 223503 (2015). doi:10.1063/1.4936793
 17. P. Peille, M. T. Ceballos, B. Cobo, J. Wilms, S. Bandler, S. J. Smith, T. Dauser, T. Brand, R. D. Hartog, J. D. Plaa, D. Barret, J.-W. D. Herder, L. Piro, X. Barcons, and E. Pointecouteau, *SPIE Astronom. Telescopes + Instr.* **9905**, 99055W (2016). doi:10.1117/12.2232011
 18. C. Hollerith, B. Simmnacher, R. Weiland, F. V. Feilitzsch, C. Isaila, J. Jochum, W. Potzel, J. Hhne, K. Phelan, D. Wernicke, and T. May, *Review of Scientific Instruments* **77**, 053105 (2006). doi: 10.1063/1.2202911
 19. J. W. Fowler, C. G. Pappas, B. K. Alpert, W. B. Doriese, G. C. O’Neil, J. N. Ullom, D. S. Swetz, *J. Low Temp. Phys.* (2018) doi: 10.1007/s10909-018-1892-5
 20. K.D. Irwin and G.C. Hilton, “Transition-edge sensors.” Cryogenic particle detection 81-97. (2005). doi: 10.1007/10933596_3
 21. D. A. Bennett, R. D. Horansky, A. S. Hoover, N. J. Hoteling, M. W. Rabin, D. R. Schmidt, D. S. Swetz, L. R. Vale, and J. N. Ullom, *Appl. Phys. Lett.* **97**, 102504, (2010). doi: 10.1063/1.3486477
 22. W. B. Doriese, K. M. Morgan, D. A. Bennett, E. V. Denison, C. P. Fitzgerald, J. W. Fowler, J. D. Gard, J. P. Hays-Wehle, G. C. Hilton, K. D. Irwin, Y. I. Joe, J. A. B. Mates, G. C. O’Neil, C. D. Reintsema, N. O. Robbins, D. R. Schmidt, D. S. Swetz, H. Tatsuno, L. R. Vale, and J. N. Ullom, *J. Low Temp. Phys.* **184**, 389 (2016). doi: 10.1007/s10909-015-1373-z
 23. D. A. Bennett, D. S. Swetz, R. D. Horansky, D. R. Schmidt, and J. N. Ullom, *J. Low Temp. Phys.* **167**, 102, (2012). doi: 10.1007/s10909-011-0431-4